Navigating the Potential Energy Surface of CdSe Magic-Sized Clusters: Synthesis and Interconversion of Atomically Precise Nanocrystal Polymorphs

Hunter H. Ripberger[#], Kyle J. Schnitzenbaumer[‡], Lily K. Nguyen[#], Dylan M. Ladd, Kelsey R. Levine, Damara G. Dayton, Michael F. Toney, Brandi M. Cossairt*[#]

Department of Chemistry, University of Washington, Seattle, Washington 98195-1700, United States

† Division of Natural Sciences and Mathematics, Transylvania University, Lexington, Kentucky 40508-1797, United States

^ Materials Science and Engineering Program, University of Colorado, Boulder, Colorado 80309, United States

§ Department of Chemical and Biological Engineering, Renewable and Sustainable Energy Institute, University of Colorado,

Boulder, Colorado 80309, United States

*Corresponding Author Email: cossairt@uw.edu

Abstract

Magic-sized clusters (MSCs) are kinetically stable, atomically precise intermediates along the quantum dot (QD) reaction potential energy surface. Literature precedent establishes two classes of cadmium selenide MSCs with QD-like inorganic cores: one class is proposed to be cation-rich with a zincblende crystal structure, while the other is proposed to be stoichiometric with a "wurtzite-like" core. However, the wide range of synthetic protocols used to access MSCs has made direct comparison of their structure and surface chemistry difficult. Furthermore, the physical and chemical relationship between MSC polymorphs has yet to be established. Here, we demonstrate that both cation-rich and stoichiometric CdSe MSCs can be synthesized from identical reagents and can be interconverted through the addition of either excess cadmium or selenium precursor. The structural and compositional differences between these two polymorphs can be contrasted using a combination of ¹H-NMR spectroscopy, x-ray diffraction, pair distribution function (PDF) analysis, inductively coupled plasma optical emission spectroscopy, and UV-vis transient absorption spectroscopy. The subsequent polymorph interconversion reactions are monitored by UV-vis spectroscopy, with evidence for an altered cluster atomic structure observed by powder x-ray diffraction and PDF analysis. This work helps simplify the complex picture of the CdSe nanocrystal landscape and provides a method to explore structure-property relationships in colloidal semiconductors through atomically precise synthesis.

Introduction

Quantum-confined semiconductor nanocrystals, or quantum dots (QDs), are ideal emitters for applications ranging from display to quantum information technologies due to their ease of synthesis, solution processability, and size-dependent optoelectronic properties¹. Because these properties result from confinement of the exciton within the bounds of the material, composition, structure, and shape of the QD play an outsized role in determining its functional properties². Over the past decade, improvements to QD synthesis have made it possible to isolate high quality ensembles with extremely narrow linewidths and high photoluminescence quantum yields^{3–5}. However, these homogenous ensembles remain heterogeneous at the atomic level, with particle-to-particle differences in quantum yields due to charging or nonuniform shell coverage appearing in even the highest quality samples^{6,7}. These differences are intrinsically tied to the typical QD growth mechanism, by which monomer continuously adds to the surface, amplifying structural differences over time⁸. Ultimately, understanding the composition, morphology, and surface coverage of QDs with atomic resolution will be necessary to successfully incorporate these materials into next-generation technologies.

In recent years, non-classical growth pathways have been recognized as playing an important role in semiconductor nanocrystal formation⁹. In special cases, including nanoplatelets and magic sized clusters (MSCs), discrete jumps in the lowest energy absorption maxima are observed, instead of a continuous redshift of the absorption features, signaling the sequential growth of larger nanocrystals without intermediate sizes^{10,11}. Of particular interest are MSCs, which are kinetically stable and atomically precise¹². MSCs are found across the periodic table, with stable structures of carbon¹³, metals¹⁴, metalloids¹⁵, and II-VI and III-V semiconductors^{16–18} well-documented and consisting of tens to hundreds of atoms.

The landscape of the CdSe MSCs is particularly well developed. The first clusters reported and structurally characterized from this class incorporated thiophenolates or selenophenolates into the inorganic core (**Figure 1A**, top left) leading to MSCs rich in anions and optoelectronic properties dominated by the ligands^{19–22}. On the other hand, a series of cadmium-rich MSCs, first synthesized by Kudera et al.¹⁰, were structurally characterized by the Owen group through surface

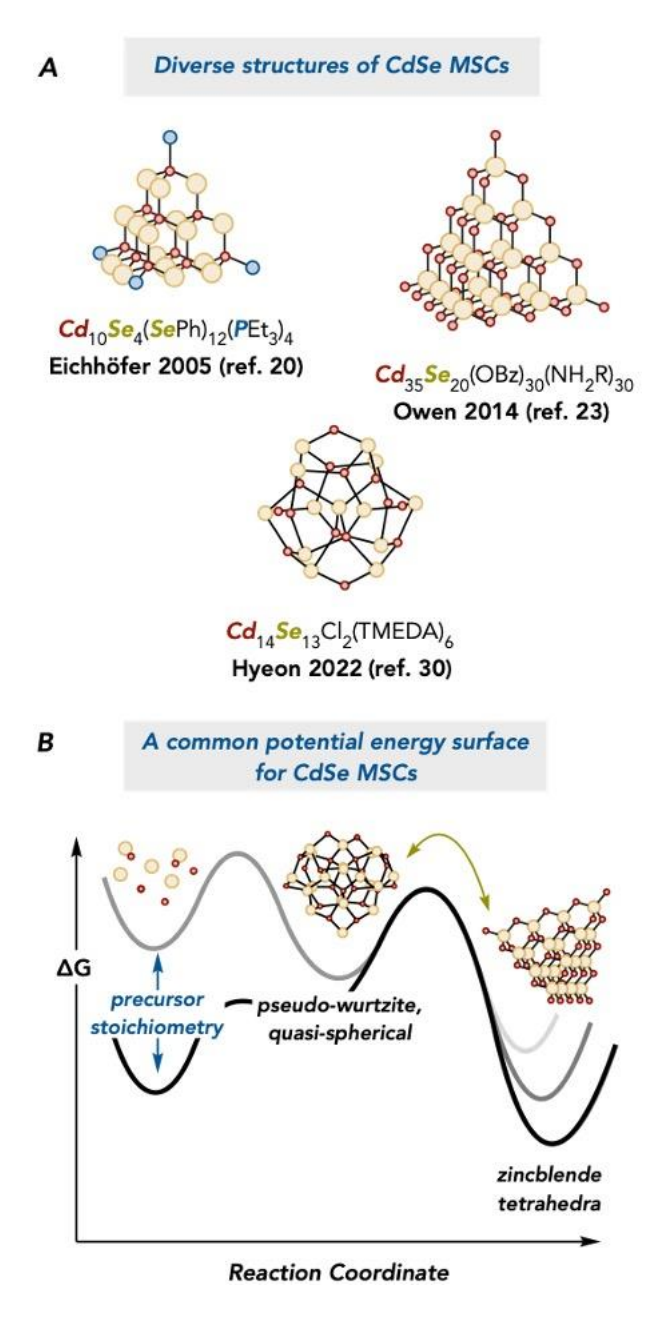


Figure 1: Diverse structures of CdSe magic sized clusters (MSCs). (A) Reported single crystal XRD structures of various CdSe MSCs (only Cd and Se shown). (B) *Hypothesis*: Distinct classes of MSCs are connected in chemical space through well-defined reactions.

passivation with benzoate and alkylamine ligands (**Figure 1A**, top right)^{23,24}. This stoichiometry more closely mimics the composition and surface environment of QDs, which are often demonstrated to be cationrich²⁵. The disclosed single crystal XRD structure and PDF analysis showed that all three of the MSCs have a tetrahedral geometry, with lowest energy absorption maxima at either 350, 380, or 408 nm. For both anion-rich and cationrich compositions, adamantane-like cages of cation and anion mirror the zincblende crystal structure of bulk cadmium selenide.

Separately, amine-capped CdSe MSCs with stoichiometric compositions (nearly) $Cd_{13}Se_{13}$ or $Cd_{14}Se_{13}$ were reported by Buhro and Hyeon in the synthesis of lamellar assemblies and nanosheets^{26–29}. The single crystal XRD structure of this cluster was disclosed in 2022 by Hyeon and coworkers, highlighting its markedly different structure from earlier reported MSCs – its quasi-spherical arrangement of Cd and Se atoms resembles a compressed wurtzite lattice (Figure 1A, bottom)³⁰. A larger MSC in this family has also been reported, with proposed compositions of $Cd_{33}Se_{33}^{31}$, $Cd_{34}Se_{34}^{29,31-33}$, $Cd_{34}Se_{33}^{30}$, $Cd_{35}Se_{28}^{24}$. In each of these reports, the lowest energy absorption maximum of the species is

approximately 420 nm, implying that these clusters have the same internal structure. Owen most thoroughly characterized this cluster in one particular synthesis, documenting a surface coverage

of 1:1 benzoate:dodecylamine ligands and a molecular weight of approximately 10400 g/mol. Hyeon also reported that this larger MSC can be synthesized from the smaller, $Cd_{14}Se_{13}$ cluster, which implies that it is likely to have the same pseudo-wurtzite internal structure³⁰. However, single crystal XRD characterization has remained elusive.

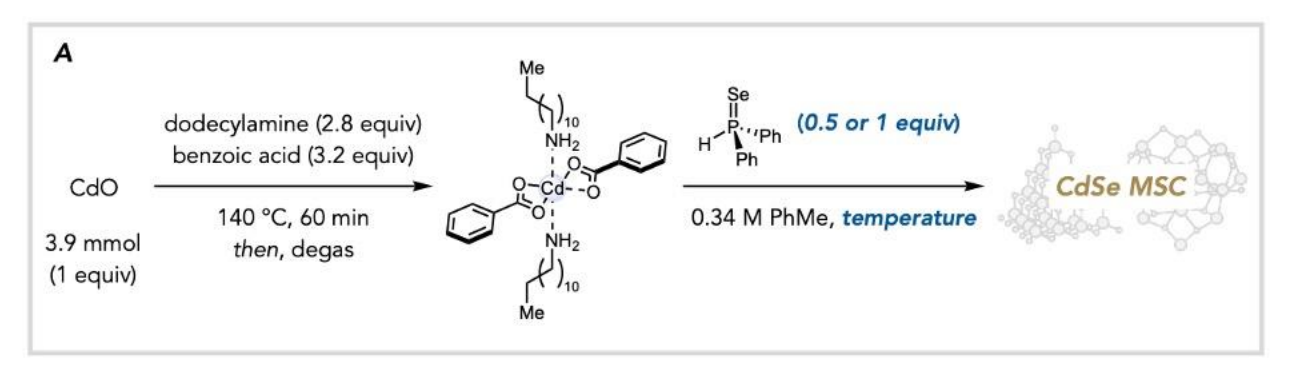
These overlapping reports highlight the complex nature of the CdSe potential energy surface, with each MSC family, and sometimes identical clusters, accessed by different synthetic routes. Furthermore, while it is established that a successful MSC synthesis requires high concentrations³⁴ and highly reactive precursors³⁵, other contributing variables, such as precursor stoichiometry, have not been as thoroughly probed. As the synthesis of nanocrystals with atomic precision grows more important, clear design principles to efficiently access these structures are necessary.

In considering the state-of-the-art, we questioned whether a streamlined route to access both cation-rich and stoichiometric CdSe MSCs from the same precursors was possible (**Figure 1B**). We could then make concrete comparisons between the structures, and, in particular, more convincingly show that the large, stoichiometric cluster possesses a pseudo-wurtzite core structure. In this report, we demonstrate the realization of these goals. We first synthesize a series of previously reported cation-rich and stoichiometric CdSe MSCs from cadmium benzoate and diphenylphosphine selenide precursors by altering the stoichiometric ratio of the reagents. We characterize the structure and composition of the MSCs using powder x-ray diffraction (XRD), pair distribution function (PDF) analysis, inductively coupled plasma optical emission spectrometry (ICP-OES), ¹H-NMR spectroscopy, and steady state and transient UV-vis absorption spectroscopy. This suite of characterization tools demonstrates that the stoichiometric and cation-rich inorganic core structures are fundamentally different. Finally, we demonstrate that the two families of MSCs can be interconverted through the addition of either excess cadmium or selenium precursor, illustrating that these two structures are connected on the same potential energy surface.

Results and Discussion

Synthesis and Characterization of CdSe MSCs

For the following discussion, a given MSC is referred to as $CdSe_{xnm}$, with "x nm" referring to the wavelength of its lowest energy absorption maximum. We first searched for a bottom-up procedure that could reliably yield both stoichiometric and cation-rich MSCs with identical ligands (Figure 2A). After some screening of cadmium and selenium precursors, we found that the stoichiometric $CdSe_{420 nm}$ MSC could be synthesized on gram scale with some modifications to the procedure of Cossairt and Owen²⁴. This procedure utilizes the *in situ* formation of cadmium benzoate and 1 equivalent diphenylphosphine selenide (DPPSe) as Cd and Se precursors, and it yields a golden yellow solid with a strong, lowest energy absorption feature centered at 420 nm (Figure 2B). Key to maintaining reproducible yields, narrow absorption linewidths, and colloidal stability was a gentle workup – excessive crash-outs with acetonitrile or high centrifugation rates led to subsequent poor solubility (Figure S11). Furthermore, rapid mixing of the two precursor solutions *via* cannula transfer, a lower reaction temperature to form the cadmium precursor, and dilution of the cadmium precursor with toluene to aid stirring were all found to positively affect the reproducibility of the MSC formation (see SI for full synthesis and workup procedures).



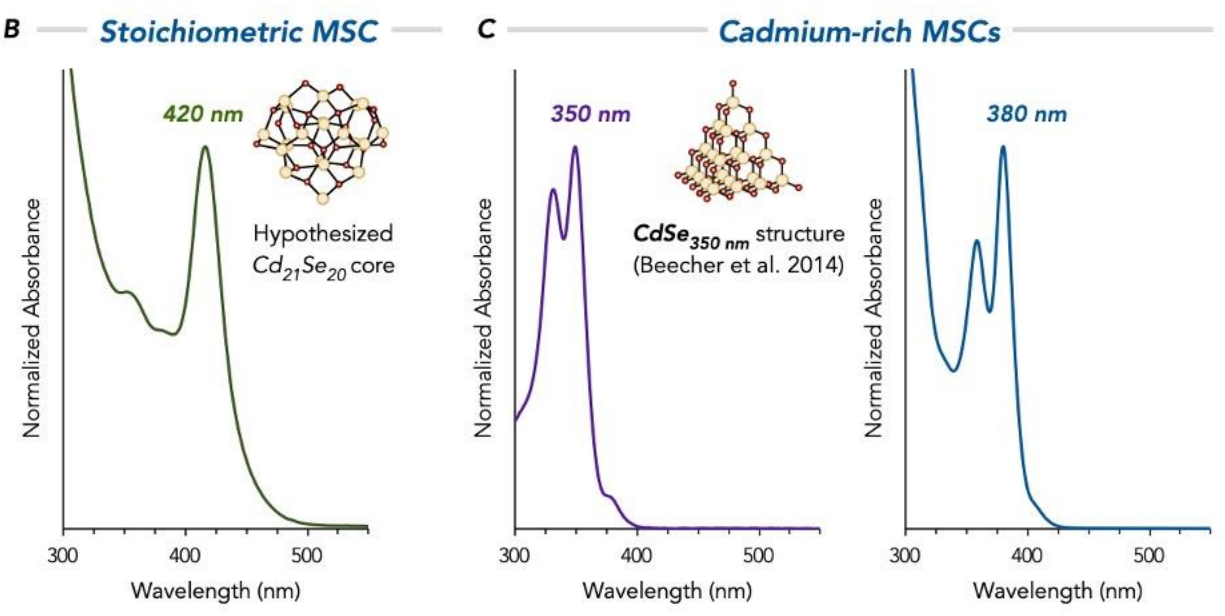


Figure 2: Synthesis of stoichiometric and cation-rich CdSe MSCs from identical precursors. (A) Procedure for the synthesis of CdSe MSCs. (B) UV-vis absorption spectrum of purified *CdSe*_{420 nm}. *Conditions*: 1 equiv DPPSe, 45 °C. (C) UV-vis absorption spectrum of purified *CdSe*_{350 nm} (left) and *CdSe*_{380 nm} (right). *Conditions*: 0.5 equiv DPPSe, room temperature (*CdSe*_{350 nm}) or 45–80 °C (*CdSe*_{380 nm}).

With a reproducible synthesis of *CdSe*_{420 nm} in hand, we found that by decreasing the stoichiometry of DPPSe from 1 to 0.5 equivalents, we could alternatively access a gram-scale synthesis of the cation-rich, tetrahedral MSC *CdSe*_{350 nm} reported by Beecher et al. as a waxy, white solid (**Figure 2C**, left)²³. Notably, a small amount of the next largest tetrahedral cluster, *CdSe*_{380 nm}, forms upon isolating purified *CdSe*_{350 nm} from solution at room temperature. By conducting the original synthesis at 45 °C, a mixture of *CdSe*_{350 nm} and *CdSe*_{380 nm} instead forms within two hours in an approximately 2:1 ratio of MSCs (**Figure S7**). Isolating this mixture from byproducts and resubjecting to heating at 80 °C fully converts these clusters into *CdSe*_{380 nm}, which

can be separated and isolated from the next tetrahedron in the series (*CdSe408 nm*) via size selective precipitation (**Figure 2C**, right).

We next characterized the compositional and structural differences between these two families of MSCs. Elemental analysis via ICP-OES showed that the Cd:Se ratios found in $CdSe_{420~nm}$ and $CdSe_{350~nm}$ were (1.02 ± 0.06) :1 and (1.75 ± 0.04) :1, respectively, highlighting their stoichiometric or cation-rich compositions. This measured Cd:Se ratio for $CdSe_{350~nm}$ is within error of the theoretical Cd:Se ratio for a composition of $Cd_{35}Se_{20}$ $(1.75:1)^{23}$. Additionally, the measured Cd:Se ratio for $CdSe_{420~nm}$ is within error of most previous literature reports of CdSe MSC compositions with an absorption maximum of approximately 420 nm, including $Cd_{33}Se_{33}^{31}$, $Cd_{34}Se_{34}^{29,31-33}$, and $Cd_{34}Se_{33}^{30}$.

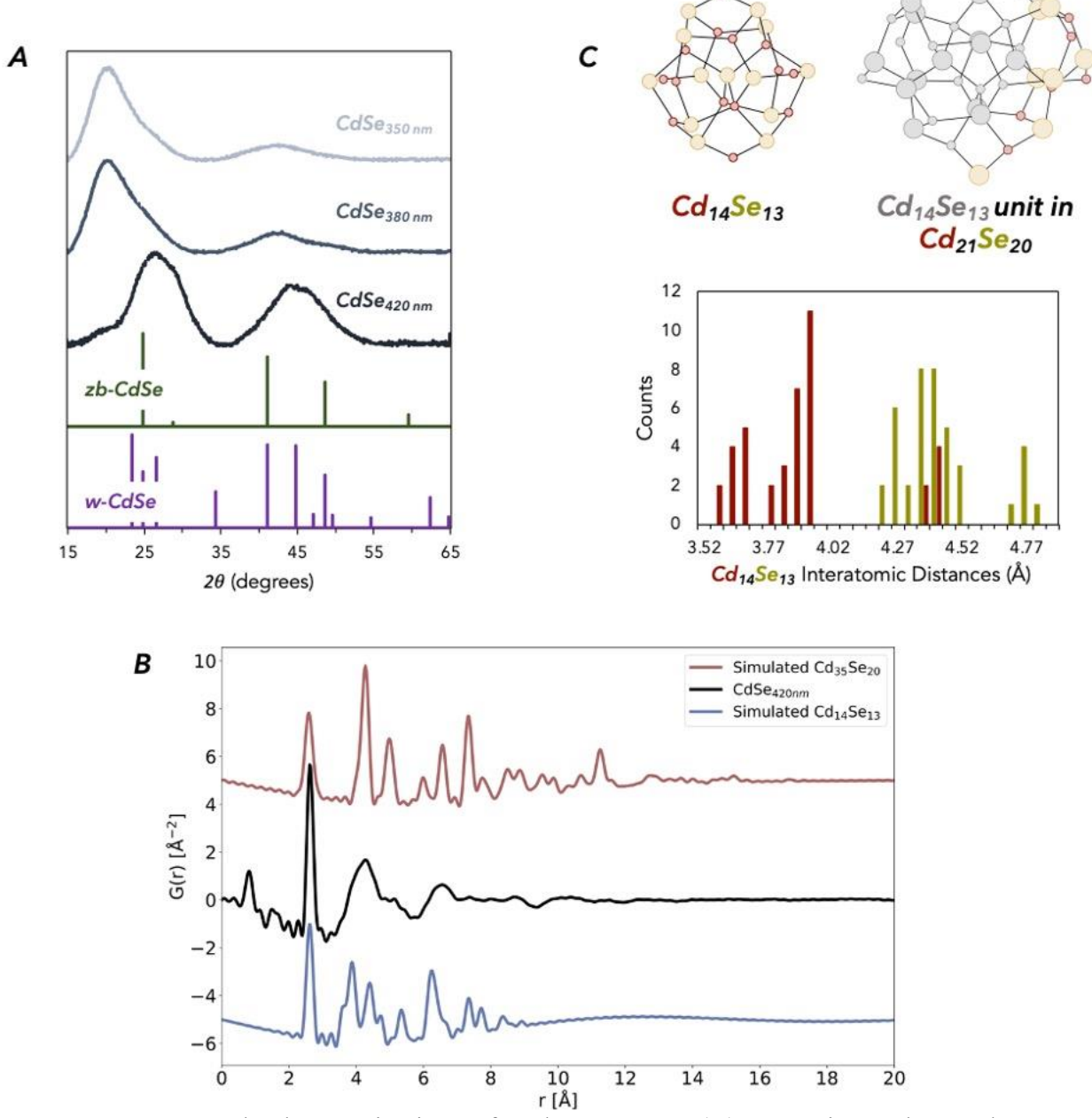


Figure 3: Structural characterization of CdSe MSCs. (A) Experimental powder x-ray diffractograms referenced to bulk zincblende and wurtzite-CdSe. (B) Experimental PDF for $CdSe_{420 nm}$ compared to simulated PDFs (offset) for each reported MSC type (refs. 23 and 30). (C) Histogram of Cd-Cd (red) and Se-Se (yellow) interatomic distances from the single crystal XRD structure of $Cd_{14}Se_{13}$ (ref. 30). Illustrations of $Cd_{14}Se_{13}$, as well as a $Cd_{14}Se_{13}$ unit inside of a larger $Cd_{21}Se_{20}$ unit – the hypothesized core structure for $CdSe_{420 nm}$.

Powder x-ray diffraction was then used to initially delineate the structures of these MSCs, and the diffraction patterns of *CdSe*_{350 nm}, *CdSe*_{380 nm}, and *CdSe*_{420 nm} are shown in **Figure 3A**. While the diffractogram peaks are broad, there are several distinct features in the patterns of

CdSe_{350 nm} and CdSe_{380 nm} versus that of CdSe_{420 nm}. With both CdSe_{350 nm} and CdSe_{380 nm}, a large peak at approximately 20° 2θ and a shoulder at 25° 2θ dominate the diffraction patterns. At higher values of 2θ, two peaks are seen at 42° and 47° 2θ that are most visible in the diffractogram of CdSe_{380 nm}. The positions of these peaks match most closely to zincblende CdSe (zb-CdSe, Figure 3A green trace), which is unsurprising, since single crystal XRD has previously shown that the structure of CdSe_{350 nm} with *n*-butylamine ligands was a zincblende tetrahedron²³. Additionally, the peak at 20° was recently characterized in InP quantum dots by Alivisatos and coworkers as corresponding to ordered packing of straight chain alkyl carboxylates along the zincblende surface (111) facet³⁶. Its presence in the diffractograms of CdSe_{350 nm} and CdSe_{380 nm} can be rationalized as dodecylamine ligands ordering along the (111) facet of the tetrahedra.

On the other hand, the broad peaks in the diffractogram of CdSe_{420 nm} are at different positions than those seen for CdSe_{350 nm} and CdSe_{380 nm} (Figure 3A, bottom). The peak at 20° 20 is present but diminished, when compared to the corresponding peak in the diffractograms of $CdSe_{350 nm}$ and $CdSe_{380 nm}$. The relative maximum in the lower 20 region also appears to be the sum of at least two peaks near 26° and 28° 20, while the higher 20 region features a broad peak with a maximum centered at approximately 45° 2θ. While the peaks on their own do not match precisely with known CdSe crystal phases, the peak at 45° 20 in particular is reminiscent of wurtzite CdSe (w-CdSe, **Figure 3A**, purple trace)³⁷. The absence of the ordered ligand peak at 20° 2θ could suggest that CdSe_{420 nm} has a quasi-spherical morphology, since this shape is characterized by high surface curvature that precludes efficient ligand packing. This notion is supported by comparing qualitative differences in the ¹H-NMR spectra of *CdSe*_{350 nm} and CdSe_{420 nm} (Figure S5 and Figure S12, respectively). While both spectra show broadened benzoate and dodecylamine proton signals characteristic of bound ligands³⁸, the degree of broadening varies between the two MSCs, with the peaks of CdSe_{350 nm} appearing much sharper than those of *CdSe420 nm*. Prior literature reports have characterized the MSCs as approximately the same size 23,24 (calculated edge length of 1.7 nm for *CdSe*_{350 nm} and measured diameter of 1.5 \pm 0.5 nm for CdSe_{420 nm}); therefore, the difference in peak broadness could be rationalized by differences in morphology. While the quasi-spherical shape of CdSe_{420 nm} allows for ligand protons to sample a wider range of environments, the tetrahedral structure of CdSe_{350 nm} results in ordered ligand packing that restricts molecular motions and exchange equilibria that manifest as broadened NMR spectrum peaks.

To gain more concrete information about the structural differences between the MSCs, we next turned to pair distribution function (PDF) analysis from x-ray total scattering data of $CdSe_{420 nm}$. The reduced pair distribution function G(r) (shown for $CdSe_{420 nm}$ in Figure 3B) is a weighted probability distribution of real space distances between atomic pairs, and thus it is a powerful descriptor of atomic local order unique to each MSC³⁹. Simulating G(r) for the reported structures of the tetrahedron $CdSe_{350 \text{ nm}}^{23}$ and the quasi-spherical MSC $Cd_{14}Se_{13}^{30}$ (blue line), we can attribute peaks in G(r) as Cd-Se, Cd-Cd, and Se-Se interatomic distances to support structural assignment of $CdSe_{420 nm}^{40}$. Key features of the simulated G(r) for the tetrahedral $Cd_{35}Se_{20}$ G(r)include: 1) a sharp peak representing the nearest neighbor Cd-Se distance of 2.60 Å, 2) closely overlapped peaks for Cd-Cd and Se-Se at 4.24 Å and 4.26 Å respectively, and 3) a sharp peak at 5.1 Å representing uniform third-nearest neighbor Cd-Se pairs. While $Cd_{14}Se_{13}$ exhibits a similar nearest neighbor Cd-Se peak at 2.61 Å, Cd-Cd average distances in Cd₁₄Se₁₃ occur in three distinct populations – 3.64, 3.87, and 4.39 Å – and average Se-Se distances are grouped near 4.39 or 4.77 Å (Figure 3C). The experimental G(r) for $CdSe_{420 nm}$ exhibits a first Cd-Se peak at 2.62 Å and a grouping of overlapping Cd-Cd, Se-Se peaks from approximately 3.6-4.6 Å and lacks a welldefined third-nearest neighbor Cd-Se peak. Overall, the measured PDF of CdSe420 nm shows a cluster structure more closely resembling the quasi-spherical/pseudo-wurtzite MSC type compared to the zincblende tetrahedron. A final insight gained from the PDF is the relative size of clusters, as pair distances in G(r) do not exceed the diameter of the cluster. In Figure 3B, the size differences of MSC types are seen by peaks of $Cd_{35}Se_{20}$ extending further in real space while the smaller $Cd_{14}Se_{13}$ cluster only possesses pair distances to approximately 9 Å. The extended oscillations in G(r) of $CdSe_{420 nm}$ tentatively suggest a particle diameter larger than $Cd_{14}Se_{13}$, but remains uncertain without well-defined peaks at higher values of r and guaranteed homogeneity of the sample.

The structural analysis presented here allows us to propose that $CdSe_{420 nm}$ is a larger, stoichiometric cluster within the same structural family as $Cd_{14}Se_{13}$ (such as $Cd_{21}Se_{20}$ in **Figure 3C**). This $Cd_{21}Se_{20}$ core is proposed to be identical to previously characterized pseudo-wurtzite MSCs $In_{37}P_{20}^{41}$ and $Cd_{37}S_{20}^{42}$, when the excess metal cations are removed. To further support this hypothesis, we generated structural models of $Cd_{21}Se_{20}$ and $Cd_{37}Se_{20}$ from the single crystal XRD structure of $In_{37}P_{20}^{41}$ and simulated the PDF (Figures **S17** and **S18**). The $Cd_{21}Se_{20}$ structure was capped with two chloride ligands for charge balance and subjected to DFT geometry optimization

using Gaussian⁴³, while the $Cd_{37}Se_{20}$ structure was left as is. While both PDFs resemble the experimental PDF of $CdSe_{420 \ nm}$ and elemental analysis via ICP-OES suggests a nearly stoichiometric composition, the peak intensities, peak positions, and MSC size in the simulated PDF of $Cd_{37}Se_{20}$ match the experimental PDF quite closely. The observed differences in the PDFs of $Cd_{21}Se_{20}$ and $Cd_{37}Se_{20}$ could suggest that coordinating ligands, which were not included in the models, play an important role in the geometry of these structures, experimentally resulting in shorter interatomic distances and a particle size better captured by the $Cd_{37}Se_{20}$ model. Nevertheless, these simulations provide additional evidence that $CdSe_{420 \ nm}$ possesses a pseudowurtzite structure that is analogous to the InP MSC previously characterized by the Cossairt lab⁴¹.

Contrasting the Photophysics of Structurally Distinct MSCs

Evidence that these structural and morphological differences between the clusters affect electronic structure can be seen in the distinctly different absorption profiles (Figure 2 and Figure 4A-C). While both *CdSe*_{350 nm} and *CdSe*_{380 nm} exhibit prominent double excitonic features in their respective UV-vis absorption spectra, the higher energy absorption features of *CdSe*_{420 nm} are much lower in intensity. Having established the structural and morphological differences between the two MSC families, one might expect deviations in the emergent behavior, such as photophysics, of the cluster families. To elucidate the photophysical consequences of the structural and morphological differences, we use transient absorption spectroscopy, a technique with a robust history of use examining QD systems. We find that the pseudo-wurtzite stoichiometric MSC exhibits different photophysics than the zincblende, tetrahedral MSCs, which exhibit characteristics analogous to CdSe QDs.

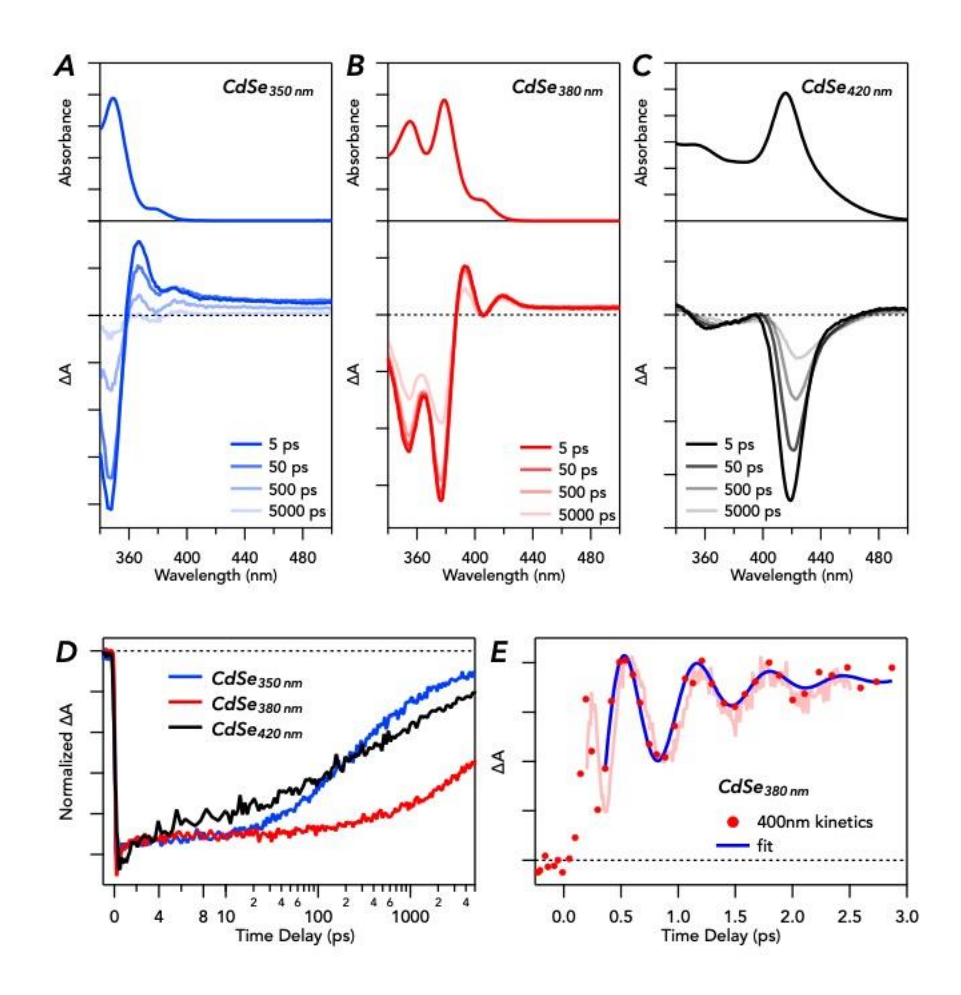


Figure 4: Summary of transient absorption on CdSe MSCs. Linear and transient absorption spectra of (A) CdSe_{350 nm}, (B) CdSe_{380 nm}, and (C) CdSe_{420 nm}. (D) Transient absorption kinetics of the lowest energy electronic transition bleach for CdSe_{350 nm}, CdSe_{380 nm}, and CdSe_{420 nm} following excitation at 342, 373, or 400 nm, respectively. (E) CdSe_{380 nm} transient absorption kinetics at 400 nm following excitation of the lowest energy absorption feature and fit of the data as described in the text/SI.

Transient absorption spectra of *CdSe*_{350 nm}, *CdSe*_{380 nm}, and *CdSe*_{420 nm} at 5, 50, 500, and 5000 ps following excitation of the lowest energy absorption feature are shown in **Figure 4A-C**. Also shown for comparative purposes are the respective linear absorption spectra. While the most prominent feature of the transient spectra for all three samples is the bleach of the lowest energy absorption feature in the linear spectrum, there are several notable differences between the zincblende, tetrahedral and the pseudo-wurtzite, stoichiometric MSCs. Transient spectra of the zincblende *CdSe*_{380 nm} MSC exhibit features often associated with CdSe QDs^{44,45}, such as a prominent bleach of the higher energy absorption feature at 350 nm and an induced absorption feature on the red-edge of the lowest energy bleach at 390 nm. The linear absorption of the sample

indicates the presence of small amounts of the next largest size tetrahedral cluster, *CdSe*_{408 nm}, and these same bleach and induced absorption features can be seen in the transient spectra at 405 nm and 420 nm, respectively. The transient spectra of the zincblende *CdSe*_{350 nm} MSC also exhibit a narrowband induced absorption feature at 370 nm, though the broadband probe lacks sufficient intensity to investigate bleaches of higher energy features in the linear absorption spectrum. In CdSe QDs, transient bleaches such as those observed here are dominated by band edge electrons and serve as reporters of photoexcited electron population^{44,46}. The narrowband induced absorption is attributed to the Stark effect⁴⁶. This combination of spectral features has been used to distinguish between InP MSCs that exhibit QD-like behavior and those that exhibit molecular-like behavior⁴⁷.

The recovery of the lowest energy bleach is shown in the transient kinetics in **Figure 4D**. Considering the spectral similarities between the zincblende tetrahedral MSCs and CdSe QDs, we expect that the bleaches report on photoexcited electron population. This is corroborated by the observation, shown in **Figure S20**, that the recovery kinetics of the lowest energy bleach following excitation of the second lowest energy absorption exactly match that of the second lowest energy bleach following excitation of the lowest energy absorption feature.

In contrast to these features in the zincblende MSCs, the transient spectra of the pseudo-wurtzite, stoichiometric $CdSe_{420\,nm}$ MSC exhibits a very weak bleach of the higher energy absorption feature at 360 nm and the absence of an induced absorption peak to the red of the lower energy bleach. Additionally, the bleach of the lowest energy absorption feature redshifts ~30 meV over the 5 ns delay measured here. The marked departure from the spectra of the QD-like $CdSe_{350\,nm}$ and $CdSe_{380\,nm}$ make apparent that the nature of the photoexcited states for these MSC families are fundamentally different.

Our transient absorption measurements also provide some insight to phonon dynamics directly correlated with the physical structure of the MSCs. Early delay time kinetics for *CdSe_{380 nm}* are shown in **Figure 4E**. The filled circles represent kinetic data at a probe wavelength of 400 nm (the red edge of the narrowband induced absorption feature) collected at the same time delay sampling frequency as data shown in **Figure 4D** covering the full 5 ns delay window. The kinetics display oscillatory behavior, which is further confirmed when the experiment is repeated at a higher time delay sampling frequency shown in the faded solid line. These oscillations arise due to the pump pulse exciting phonon modes in the sample and have previously been shown to be sensitive to the material parameters of cadmium chalcogenide QDs and their ligand shell⁴⁸.

Figure 4E also shows a fit to the data, as outlined in the SI, which describes the oscillatory component as a damped driven harmonic oscillator. The frequency of these oscillations extracted by the fit is 53 cm⁻¹. Considering the smaller size (edge length ~ 2.1 nm) and tetrahedral shape of the CdSe_{380 nm} MSCs compared with QDs, this value compares favorably to the 20 - 30 cm⁻¹ reported for the radial breathing mode of CdSe QDs with radii ranging from 1.5 to 3 nm^{49,50}. Similar oscillatory character is observed in the kinetics of CdSe_{380 nm} MSCs following excitation of the second lowest energy absorption features (54 cm⁻¹) and the *CdSe*_{350 nm} MSCs following excitation of the lowest energy absorption feature (62 cm⁻¹) as shown in Figure S21 and Figure S22, respectively. We interpret the oscillations in the transient kinetics as due to a "radial" breathing mode of the zincblende, tetrahedral MSCs analogous to those previously described in CdSe QDs^{51,52}. In contrast, no oscillations were observed at any probe wavelengths in the transient kinetics of the pseudo-wurtzite CdSe_{420 nm} MSCs. The absence of oscillatory character in the CdSe_{420 nm} kinetics could be indicative of one or both of the following: (1) Inappropriate excitonphonon coupling precluding its generation. This may arise due to the pseudo-wurtzite MSC inorganic core being less periodic than the zincblende core. (2) Critical damping of the phonon mode. Modification of the ligand shell on the same inorganic QD core has been shown to cause damping of the radial breathing mode⁴⁸. Such damping may be plausible here considering the variation in ligand ordering discussed above. Either explanation highlights markedly divergent behavior due to the structural differences between the two families of MSCs.

Conversion from Psuedo-Wurtzite to Zincblende MSCs

With the stoichiometric MSC *CdSe*_{420 nm} established as possessing a different local structure than the tetrahedral MSC series, we then moved to determine how the different CdSe cluster families are related on the reaction potential energy surface. The sequential growth of zincblende-like CdSe MSCs has been demonstrated in the literature under various conditions. Manna and coworkers reported the controlled evolution of CdSe MSCs capped with nonanoic acid and dodecylamine ligands in 2007¹⁰. In the original synthesis of *CdSe*_{350 nm} capped with *n*-butylamine ligands, Owen and coworkers showed that a mixture of *CdSe*_{350 nm} and *CdSe*_{408 nm} can be grown from a heated solution of *CdSe*_{350 nm} without exogeneous precursors. And in recent work, Norris and coworkers similarly demonstrated the sequential growth of myristate-capped zincblende CdSe MSCs through the addition of excess cadmium precursor and proposed a model

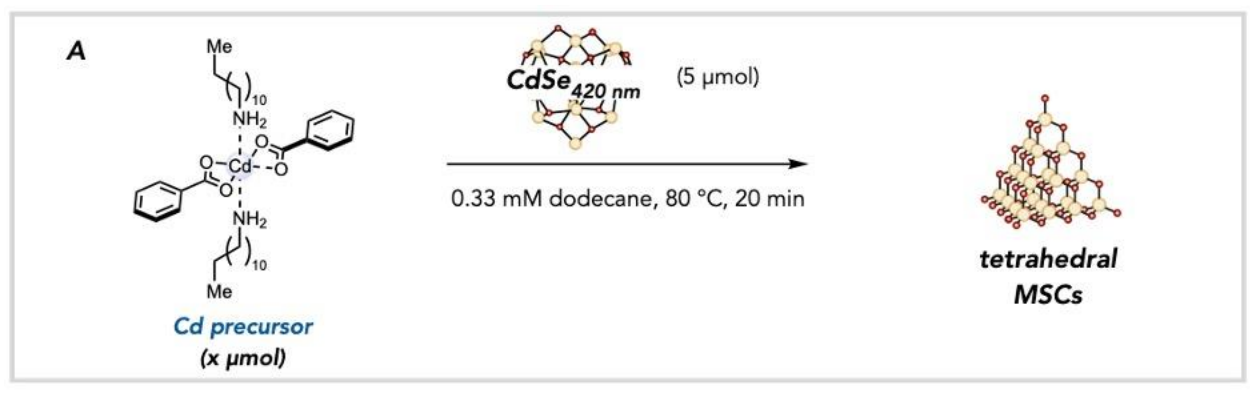
for this growth, where monomer addition to the zincblende (111) facet results in the formation of the next-largest cluster once the facet is fully passivated^{11,53}. In our hands, large zincblende MSCs, with lowest energy excitation maxima of 430 nm or 455 nm, could be grown by injecting *CdSe*_{380 nm} into heated solvent (**Figure S23** and **S24**).

Less is known about the reactivity of stoichiometric, pseudo-wurtzite clusters like $CdSe_{420 nm}$. When passivated solely by amine ligands, this cluster was demonstrated to reversibly grow from and etch into a smaller, stoichiometric cluster (with reported core makeup of either $Cd_{14}Se_{13}$ or $Cd_{13}Se_{13}$) through ligand exchange with N-alkyl- or N,N-dialkylamines^{30,32}. However, further growth into larger, atomically precise nanocrystals was not reported. Instead, nanoplatelets and lamellar aggregates formed facilely at temperatures at or slightly above room temperature^{29,32}.

We questioned whether the change to a 1:1 benzoate/amine ligand shell utilized in our synthesis of *CdSe420 nm* would alter this reported growth trajectory. It has been previously demonstrated that addition of amine to the pseudo-wurtzite, phenylacetate-capped InP MSC $In_{37}P_{20}$ promotes a rearrangement to a higher symmetry MSC $In_{35}P_{20}$ with loss of two amine-ligated indium carboxylates⁵⁴. However, titration of *CdSe420 nm* with a variety of amines led to either loss of colloidal stability (short-chain alkylamines) or L-type binding (oleylamine), with no evidence by UV-Vis absorption spectroscopy for any large-scale structural rearrangement (**Figure S25**) and no evidence by ¹H-NMR spectroscopy for displacement of cadmium benzoate or benzoic acid from the MSC surface (**Figure S26**).

On the other hand, injection of *CdSe*_{420 nm} into a solution of cadmium benzoate at 80 °C rapidly consumes the original MSC and yields a mixture of products with UV-vis absorption maxima between 400 and 455 nm, closely matching the lowest energy excitation maxima of the larger tetrahedral MSCs (**Figure 5A** and **Figure S27**). Increasing the concentration of the cadmium precursor across an order of magnitude results in more rapid consumption of *CdSe*_{420 nm} while also shifting the distribution of absorption maxima towards higher energy peaks (**Figure 5B**, left), with the lowest energy excitation maximum of *CdSe*_{350 nm} prominently featured at high cadmium benzoate concentrations (46.6 mM). The fast nature of this reaction and the many overlapping product peaks precluded our attempts to gain quantitative insight into the kinetics of this reaction through initial rates (utilizing the measured extinction coefficient of *CdSe*_{420 nm} at 418 nm²⁴), outside of the slowest reacting conditions (**Figure S37**). However, we were able to draw similar conclusions from this data by fitting each UV-vis absorption spectrum to a series of gaussians (see

SI for details). By assuming that the peak area fit to 420 nm is proportional to the concentration of $CdSe_{420 nm}$, we can extract rates for the change in peak area with time as a function of cadmium benzoate concentration. This approximation of the reaction rate increases linearly with respect to cadmium benzoate concentration – with $-dA_{420 nm}/dt$ ranging from 10^{-5} to 10^{-4} eVs⁻¹, and rate constant approximation $k = 2 \times 10^{-5}$ s⁻¹ – showing that the conversion reaction is first order in Cd precursor (Figure 5B right, and Figures S46 and S47). Additionally, due to the large difference in concentration between the MSC and Cd precursor, the reaction is pseudo-zeroth order in $CdSe_{420 nm}$ under the described conditions (Figure S38–S40).



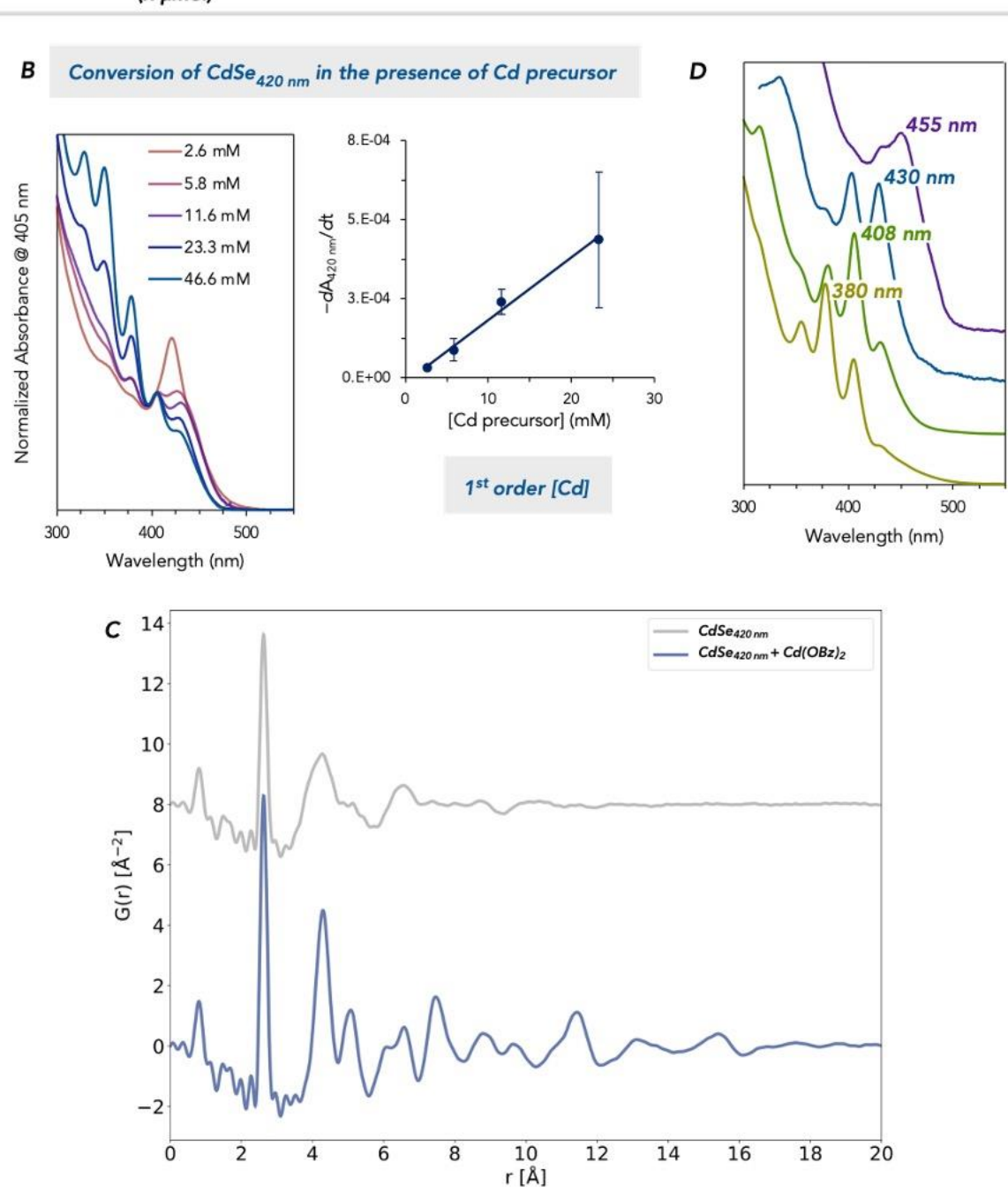


Figure 5: Addition of excess cadmium precursor to the stoichiometric MSC *CdSe*_{420 nm} yields a series of tetrahedral MSCs (*CdSe*_{350 nm}, *CdSe*_{380 nm}, *CdSe*_{408 nm}, *CdSe*_{408 nm}, and *CdSe*_{455 nm}). (A) Reaction conditions for the conversion reaction. (B) Left: Conversion reactions conducted at 80 °C with varying concentration of cadmium precursor monitored by UV-vis absorption spectroscopy, with time point at 20 minutes shown. Right: Approximated reaction rate as a function of cadmium precursor concentration. (C) Experimental PDF of *CdSe*_{420 nm} versus isolated products of *CdSe*_{420 nm} addition to 5.8 mM cadmium precursor at 100 °C (offset for visual clarity). (D) Series of tetrahedral MSCs isolated from reaction using size-selective precipitation.

Powder XRD characterization of products isolated from CdSe_{420 nm} injection into 5.8 mM cadmium benzoate solution at 100 °C demonstrates that the structure has changed from pseudowurtzite to zincblende, giving credence to the possibility that the stoichiometric cluster converts into a series of tetrahedral MSCs. (Figure S28). PDF analysis of product isolated from the same reaction conditions supports this hypothesis, with sharpened first coordination shell peaks at 2.62, 4.28, and 5.06 Å matching with zincblende interatomic distances measured from the single crystal XRD structure of $CdSe_{350 nm}$ (Figure 5C) and with the simulated PDF in Figure S19 for $Cd_{35}Se_{20}$. The structural correlation length increases from 10 to 18 Å in the converted sample, supporting the structural assignment of a larger MSC with a zincblende tetrahedral packing motif. We then confirmed the formation of zincblende-like clusters by isolating multiple species with lowest energy absorption features consistent with previously synthesized tetrahedral MSCs – $CdSe_{380 nm}$, CdSe_{408 nm}, CdSe_{430 nm}, and CdSe_{455 nm} – from the reaction of CdSe_{420 nm} with cadmium benzoate via size selective precipitation (Figure 5D). ICP-OES characterization of a sample that is majority CdSe_{430 nm} isolated from this reaction confirms that the cluster is enriched in cadmium, with a Cd:Se ratio of (1.31 ± 0.15) :1. Extrapolating from the reported composition of $CdSe_{408}$ nm $(Cd_{84}Se_{56})$, this ratio is within error of the expected composition of $CdSe_{430 \text{ nm}}$ ($Cd_{120}Se_{84}$, with a theoretical Cd:Se ratio of 1.43:1). Finally, simply injecting CdSe_{420 nm} into heated solvent without any additional precursor also promoted this transformation; however, the colloidal stability of the resulting products was significantly diminished (Figure S31).

Putting these observations together, we have substantial evidence that the stoichiometric, pseudo-wurtzite cluster undergoes a transformation with heat and cadmium precursor into a series of cation-rich tetrahedra, and we can propose the following qualitative mechanism for how this conversion reaction proceeds. Because the reaction occurs by heating with or without exogeneous cadmium benzoate, the zincblende MSCs are thermodynamically more stable than *CdSe*_{420 nm}. Furthermore, the presence of isosbestic points in the UV-vis absorption spectra taken over the

course of reaction monitoring (Figure S27) point to relatively clean conversion kinetics. Looking closer at the UV-vis absorption traces with either 5.8 or 11.6 mM cadmium benzoate, we see that the major absorption features present after 20 minutes most closely match the tetrahedral MSCs $CdSe_{408\,nm}$ and $CdSe_{430\,nm}$. Since the formation of $CdSe_{430\,nm}$ from $CdSe_{380\,nm}$ takes several hours at 80 °C (Figure S23), it must instead form directly from $CdSe_{420\,nm}$, instead of through the earlier formation of smaller tetrahedral MSCs that then ripen in line with the mechanism proposed by Norris⁵³. While it's unclear precisely how this occurs, slow fragmentation of $CdSe_{420\,nm}$ into CdSe fragments and monomers of different nuclearity during the first few minutes of heating would provide building blocks to construct the thermodynamically more stable zincblende tetrahedra.

We then considered several scenarios for why higher concentrations of Cd precursor favor smaller sized tetrahedra. One possibility is that the presence of a large excess of cadmium precursor etches the surface of larger tetrahedra, favoring the production of *CdSe*_{350 nm}. By fitting each peak to a gaussian in the experimental UV-vis absorption spectra of the reaction at different concentrations of cadmium benzoate, we can see that a decrease in the peak area at 430 nm corresponds to an equivalent increase in the peak areas at 350 nm and 330 nm (at the 300 s timepoint, **Figure S48**). Another possibility is that at higher concentrations, the cadmium precursor more effectively intercepts zincblende CdSe fragments released by the conversion of *CdSe*_{420 nm}, forming a larger population of small tetrahedra like *CdSe*_{350 nm} without etching. However, the peak area for the 430 nm peak fit in the reaction with 46.6 mM cadmium benzoate decreases as the experiment time increases, which is not the result one would expect if more of the smaller tetrahedra were being produced without consumption of the larger sizes (**Figure S49**). Either way, this series of experiments demonstrates that this collection of both stoichiometric and cation-rich MSCs is connected on the same reaction potential energy surface.

Conversion from Zincblende to a Pseudo-Wurtzite MSC

With the pseudo-wurtzite MSC *CdSe*_{420 nm} demonstrated to convert into zincblende clusters with heating and cadmium benzoate addition, we questioned whether the reverse reaction was possible as well. We hypothesized that treating a cation-rich MSC with excess selenium precursor could induce structural changes that would accommodate the increase in selenium content (**Figure 6A**). Injection of the tetrahedral MSC *CdSe*_{350 nm} into heated solution with increasing concentration of DPPSe resulted in progressively larger changes to the UV-vis absorption spectrum of the

material (**Figure 6B**). Unlike the reactions where cadmium precursor is added to the stoichiometric cluster, addition of low concentrations of DPPSe (2.6 or 3.4 mM - 8 to 10 equivalents based on moles of $CdSe_{350 nm}$) to the tetrahedral cluster does not immediately affect the absorption features, with the absorption peaks at 380 and 405 nm indicating that $CdSe_{350 nm}$ has primarily grown into larger tetrahedra under these conditions. However, increasing the selenium precursor concentration past these values results in the growth of a broad peak, initially centered at 420 nm that is further redshifted at higher concentrations.

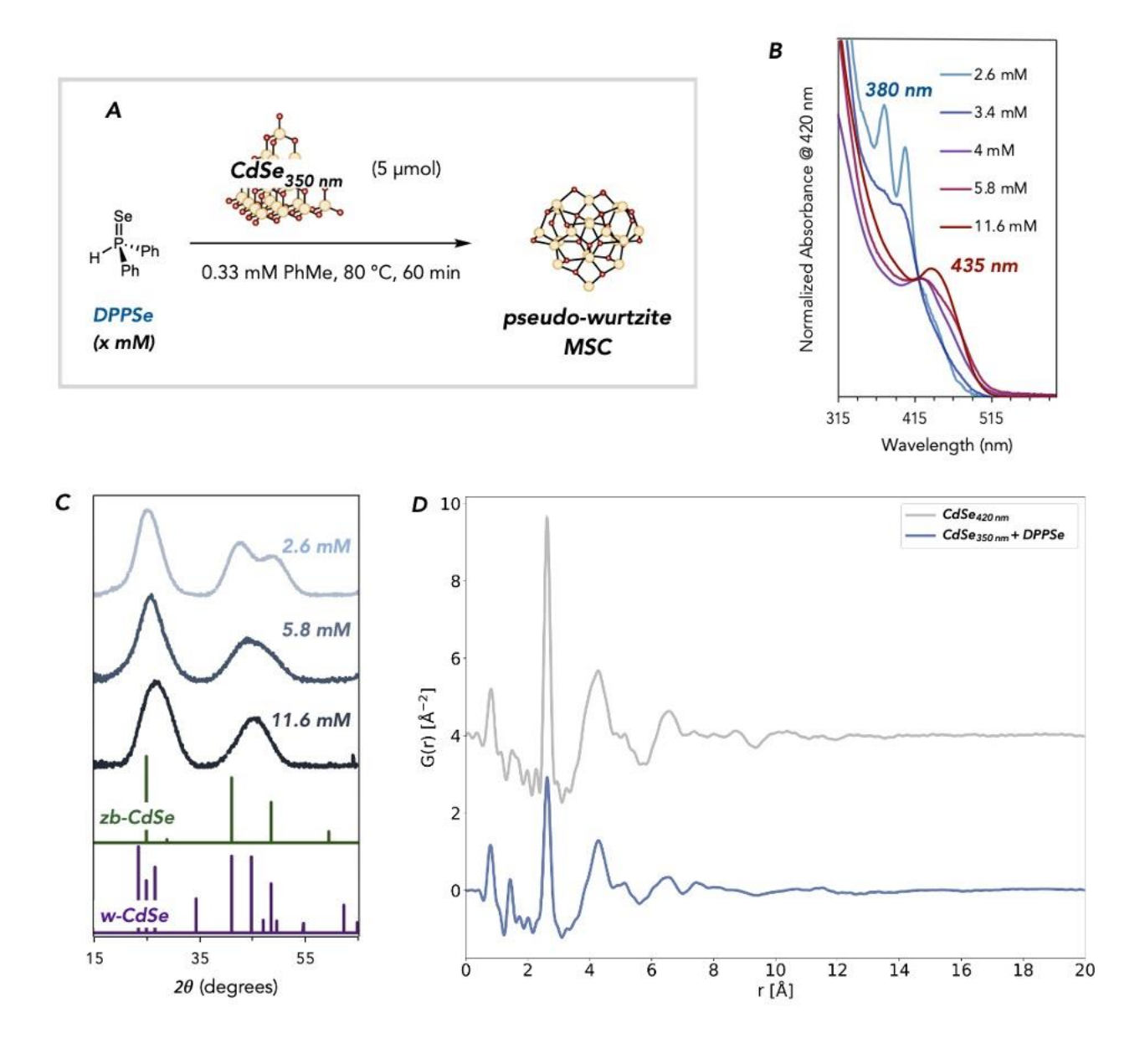


Figure 6: Addition of excess selenium precursor to the cation-rich MSC yields pseudo-wurtzite MSC. (A) Reaction conditions for the conversion reaction. (B) Conversion reactions conducted at 80 °C and varying concentration of DPPSe monitored by UV-vis absorption spectroscopy, with time point at 60 minutes shown. Right: X-ray diffractograms of isolated product from reaction with increasing [DPPSe]. (C) X-ray diffractograms of isolated product from reaction with increasing [DPPSe]. (D) Experimental PDF of *CdSe420 nm* compared to *CdSe350 nm* + DPPSe, (offset for visual clarity).

Fitting these UV-vis absorption traces in the same manner as before allows us to extract approximations for the observed rates at various concentrations of DPPSe (**Figure S36**). We calculate that the rate dependence on [DPPSe] is first order ($dA_{420 nm}/dt$ ranges from 3×10^{-5} to 9×10^{-5} eVs⁻¹ at [DPPSe] used in the reaction, with rate constant approximation $k = 8 \times 10^{-6}$ s⁻¹ – **Figures S55** and **S56**). This contrasts with the mechanism invoked for CdSe monomer formation from DPPSe and cadmium benzoate, which is proposed in the presence of amine to proceed first through a diphenylphosphinodiselenoate intermediate that implies a second order rate dependence²⁴. While byproducts associated with the reactivity of the phosphinodiselenoate intermediate are observed by ³¹P-NMR spectroscopy of the crude reaction mixture, diphenylphosphine is also formed as a substantial byproduct (**Figure S33**), which suggests an additional mechanism of reactivity. In the formation of lead selenide nanocrystals from lead(II) carboxylates and DPPSe, Krauss and coworkers suggested that DPPSe reacts with PbSe monomer in solution to yield PbSe₂ and diphenylphosphine⁵⁵. In our case, it is plausible that DPPSe reacts in this manner, since CdSe units are already present from **CdSe**_{350 nm}. Thus, a reaction order in [DPPSe] less than 2 is not out of the question for this transformation.

Finally, elemental analysis of the purified reaction sample from the reaction of $CdSe_{350 nm}$ with 11.6 mM of DPPSe showed a Cd:Se ratio of (0.64 ± 0.07) :1, highlighting that the sample has become significantly enriched in selenium. Therefore, while it's unclear from this data whether a single MSC is formed or the product contains a mixture of species, due to the broad and redshifted absorption profile compared to pristine $CdSe_{420 nm}$, we hypothesize that $CdSe_{350 nm}$ underwent a transformation from cation-rich to more stoichiometric.

To gain further insight into this transformation, we next looked at the powder XRD patterns of purified samples at different concentrations of DPPSe (**Figure 6C**). Moving from 2.6 to 11.6 mM DPPSe, we see a small shift in the low index peak to higher values of 2θ , and this peak also broadens at high concentrations of DPPSe. More pronounced changes occur in the higher

index region, where a decrease in peak intensity at 42° and 49° 20 occurs concurrently with an increase in intensity at 45° 20. These changes are reminiscent of an increase in the wurtzite-CdSe contributions to the inorganic core structure. Supporting this hypothesis is PDF analysis of the purified reaction product of *CdSe*_{350 nm} with 5.8 mM DPPSe (**Figure 6D**) showing a relative increase in intensity at interatomic distances of approximately 3.6–4.6 Å, corresponding to the pseudo-wurtzite structure type (blue trace). The similarity in peak positions between this sample and the experimental PDF of *CdSe*_{420 nm} further supports this notion (**Figure 6D**, gray trace). Thus, it is apparent that the wurtzite phase fraction increases as DPPSe equivalents used in the reaction increase.

Prior literature reports have noted similar changes in absorption spectra during CdSe MSC synthesis. Sardar and coworkers in 2012 reported the synthesis of a CdSe cluster with an absorption maximum at 422 nm using cadmium acetate and trioctylphosphine selenide precursors, with either trioctylphosphine oxide, carboxylic acid, trialkylamine, or phosphonic acid ligands⁵⁶. Under identical conditions with oleylamine ligands, MSC growth, with discrete absorption maxima at 322 nm, 350 nm, 380 nm, 404 nm, and 424 nm, was observed instead. The authors proposed that amine coordination changes the identity of the cadmium precursor, which results in the formation of different MSC families. However, the presence of amine can also alter the speciation of the Se precursors present in solution⁵⁵, leading to disproportionation of dialkylphosphine selenide impurities into diselenoates²⁴ that lower the effective stoichiometry of Se and could favor the formation of MSCs with absorption features consistent with the tetrahedral morphology instead. In another report, Yu and coworkers demonstrated a cation exchange reaction from ZnSe to CdSe MSCs⁵⁷. After addition of cadmium acetate into a solution of ZnSe MSC in cyclohexane and oleylamine, UV-vis absorption features at approximately 355 nm, 391 nm, and 417 nm grew in over time (consistent with CdSe_{350 nm}, CdSe_{380 nm}, and CdSe_{420 nm}). The researchers instead proposed that these features correspond to CdSe MSC isomers with a Cd:Se ratio of 2:1 calculated via MALDI-TOF but without definitive structural assignments. However, these spectroscopic observations aren't incongruous with our proposal, since we have demonstrated here that in the presence of exogenous precursor, a mixture of cluster morphologies can form initially before growth into a majority single structure type.

Conclusions

Here, we have shown that previously reported cation-rich and stoichiometric CdSe MSCs possess fundamentally different structure types and morphologies. Structural characterization *via* powder x-ray diffraction and PDF analysis reinforces that cation-rich MSCs have a zincblende structure that contrasts with the pseudo-wurtzite structure of stoichiometric MSCs. Morphological differences between the two MSC families also manifest in distinct surface characterization, with evidence for ordered ligand packing observed with the zincblende tetrahedra that is absent in the pseudo-wurtzite MSC. These structural and morphological differences result in different emergent photophysical properties of the MSCs that can be probed with transient absorption spectroscopy, with the zincblende tetrahedra exhibiting transient spectral features and time-resolved phonon dynamics similar to those reported in CdSe QDs.

This suite of experiments has additionally demonstrated that the growth trajectories of these MSCs are not divergent. They are connected in chemical space and can be interconverted through the inclusion of the appropriate cation or anion precursor (Figure 1B). With cadmium benzoate and DPPSe as cadmium and selenium precursors, choice of reagent stoichiometry will result in the formation of either the pseudo-wurtzite or the zincblende MSC. Isolation of the smallest sized zincblende MSC, CdSe_{350 nm}, and redissolution in heated solvent converts this cluster sequentially and discretely into larger tetrahedra, as previously shown in the literature 10,23,53. Isolation of the pseudo-wurtzite MSC CdSe_{420 nm} and reinjecting into heated solvent with excess cadmium precursor rapidly fragments and rearranges the cluster into multiple differently sized tetrahedra. Increasing the concentration of cadmium benzoate shifts the equilibrium of tetrahedra formed towards smaller sizes, highlighting that the reaction potential energy surface connecting the tetrahedra can be potentially traversed in reverse at the appropriate concentration through etching. Furthermore, the fact that conversion from the pseudo-wurtzite to zincblende MSCs also occurs with only heating demonstrates that this reaction is thermodynamically downhill. Finally, addition of DPPSe to CdSe_{350 nm} can drive the equilibrium position back towards the pseudo-wurtzite MSC, with more wurtzite character in the crystal structure observed at higher concentrations of DPPSe.

Fine control of the structure of atomically precise nanomaterials is essential for their integration into next-generation technologies. This work illustrates that control can be accomplished in CdSe MSCs either through the *de novo* synthesis of distinct polymorphs or by

converting between polymorphs in a regular fashion. The analysis of the nature and conversion mechanisms of MSC polymorphs presented here opens the door to a wider exploration of the structure of atomically precise semiconductors.

Acknowledgments

This work was supported by the National Science Foundation under grant CHE-2107237. PDF characterization was completed in collaboration with support from the National Science Foundation under Grant No. DMR-2019444. Part of this work was conducted at the Washington Nanofabrication Facility / Molecular Analysis Facility, a National Nanotechnology Coordinated Infrastructure (NNCI) site at the University of Washington with partial support from the National Science Foundation *via* awards NNCI-1542101 and NNCI-2025489. X-ray total scattering experiments were completed at Beamline 28-ID-1 (PDF) of the National Synchrotron Light Source II, a U.S. Department of Energy (DOE) Office of Science User Facility operated for the DOE Office of Science by Brookhaven National Laboratory under Contract No. DE-SC0012704.

Supporting Information

Electronic supplementary information is available including general procedures and additional data related to the synthesis and characterization of CdSe magic-sized clusters, x-ray pair distribution function analysis, transient absorption spectroscopy, and conversion reactions of CdSe magic-sized clusters.

References

- García de Arquer, F. P.; Talapin, D. V.; Klimov, V. I.; Arakawa, Y.; Bayer, M.; Sargent,
 E. H. Semiconductor Quantum Dots: Technological Progress and Future Challenges.
 Science 2021, 373 (6555):eaaz8541. https://doi.org/10.1126/science.aaz8541.
- (2) Burda, C.; Chen, X.; Narayanan, R.; El-Sayed, M. A. Chemistry and Properties of Nanocrystals of Different Shapes. *Chem. Rev.* **2005**, *105* (4), 1025–1102. https://doi.org/10.1021/cr030063a.
- (3) Chen, O.; Zhao, J.; Chauhan, V. P.; Cui, J.; Wong, C.; Harris, D. K.; Wei, H.; Han, H. S.; Fukumura, D.; Jain, R. K.; Bawendi, M. G. Compact High-Quality CdSe-CdS Core-Shell Nanocrystals with Narrow Emission Linewidths and Suppressed Blinking. *Nat. Mater.*

- **2013**, 12 (5), 445–451. https://doi.org/10.1038/nmat3539.
- (4) Nagaoka, Y.; Tan, R.; Li, R.; Zhu, H.; Eggert, D.; Wu, Y. A.; Liu, Y.; Wang, Z.; Chen, O. Superstructures Generated from Truncated Tetrahedral Quantum Dots. *Nature* **2018**, *561* (7723), 378–382. https://doi.org/10.1038/s41586-018-0512-5.
- Yu, P.; Cao, S.; Shan, Y.; Bi, Y.; Hu, Y.; Zeng, R.; Zou, B.; Wang, Y.; Zhao, J. Highly Efficient Green InP-Based Quantum Dot Light-Emitting Diodes Regulated by Inner Alloyed Shell Component. *Light Sci. Appl.* 2022, 11:162. https://doi.org/10.1038/s41377-022-00855-z.
- (6) Mcbride, J.; Treadway, J.; Feldman, L. C.; Pennycook, S. J.; Rosenthal, S. J. Structural Basis for near Unity Quantum Yield Core/Shell Nanostructures. *Nano Lett.* **2006**, *6* (7), 1496–1501. https://doi.org/10.1021/nl060993k.
- (7) Orfield, N. J.; McBride, J. R.; Wang, F.; Buck, M. R.; Keene, J. D.; Reid, K. R.; Htoon, H.; Hollingsworth, J. A.; Rosenthal, S. J. Quantum Yield Heterogeneity among Single Nonblinking Quantum Dots Revealed by Atomic Structure-Quantum Optics Correlation. ACS Nano 2016, 10 (2), 1960–1968. https://doi.org/10.1021/acsnano.5b05876.
- (8) Murray, C. B.; Norris, D. J.; Bawendi, M. G. Synthesis and Characterization of Nearly Monodisperse CdE (E = S, Se, Te) Semiconductor Nanocrystallites. *J. Am. Chem. Soc.* **1993**, *115* (19), 8706–8715. https://doi.org/10.1021/ja00072a025.
- (9) Lee, J.; Yang, J.; Kwon, S. G.; Hyeon, T. Nonclassical Nucleation and Growth of Inorganic Nanoparticles. *Nat. Rev. Mater.* 2016, 1:16034. https://doi.org/10.1038/natrevmats.2016.34.
- (10) Kudera, S.; Zanella, M.; Giannini, C.; Rizzo, A.; Li, Y.; Gigli, G.; Cingolani, R.; Ciccarella, G.; Spahl, W.; Parak, W. J.; Manna, L. Sequential Growth of Magic-Size CdSe Nanocrystals. *Adv. Mater.* 2007, 19 (4), 548–552. https://doi.org/10.1002/adma.200601015.
- (11) Pun, A. B.; Mazzotti, S.; Mule, A. S.; Norris, D. J. Understanding Discrete Growth in Semiconductor Nanocrystals: Nanoplatelets and Magic-Sized Clusters. *Acc. Chem. Res.* 2021, 54 (7), 1545–1554. https://doi.org/10.1021/acs.accounts.0c00859.
- (12) Dance, I. G.; Choy, A.; Scudder, M. L. Syntheses, Properties, and Molecular and Crystal Structures of (Me4N)4[E4M10(SPh)16] (E = S, Se; M = Zn, Cd): Molecular Supertetrahedral Fragments of the Cubic Metal Chalcogenide Lattice. *J. Am. Chem. Soc.*

- 1984, 106 (21), 6285–6295. https://doi.org/10.1021/ja00333a030.
- (13) Kroto, H. W.; Heath, J. R.; O'Brien, S. C.; Curl, R. F.; Smalley, R. E. C60: Buckminsterfullerene. *Nature* **1985**, *318* (6042), 162–163. https://doi.org/10.1038/318162a0.
- (14) Jin, R.; Zeng, C.; Zhou, M.; Chen, Y. Atomically Precise Colloidal Metal Nanoclusters and Nanoparticles: Fundamentals and Opportunities. *Chem. Rev.* **2016**, *116* (18), 10346–10413. https://doi.org/10.1021/acs.chemrev.5b00703.
- (15) Schnöckel, H. Structures and Properties of Metalloid Al and Ga Clusters Open Our Eyes to the Diversity and Complexity of Fundamental Chemical and Physical Processes during Formation and Dissolution of Metals. *Chem. Rev.* **2010**, *110* (7), 4125–4163. https://doi.org/10.1021/cr900375g.
- (16) Friedfeld, M. R.; Stein, J. L.; Ritchhart, A.; Cossairt, B. M. Conversion Reactions of Atomically Precise Semiconductor Clusters. *Acc. Chem. Res.* 2018, 51 (11), 2803–2810. https://doi.org/10.1021/acs.accounts.8b00365.
- (17) Zhang, J.; Bu, X.; Feng, P.; Wu, T. Metal Chalcogenide Supertetrahedral Clusters: Synthetic Control over Assembly, Dispersibility, and Their Functional Applications. *Acc. Chem. Res.* 2020, 53 (10), 2261–2272. https://doi.org/10.1021/acs.accounts.0c00381.
- (18) Bootharaju, M. S.; Baek, W.; Lee, S.; Chang, H.; Kim, J.; Hyeon, T. Magic-Sized Stoichiometric II–VI Nanoclusters. *Small* **2021**, *17* (27), 2002067. https://doi.org/10.1002/smll.202002067.
- (19) Behrens, S.; Bettenhausen, M.; Deveson, A. C.; Eichhöfer, A.; Fenske, D.; Lohde, A.; Woggon, U. Synthesis and Structure of the Nanoclusters
 [Hg32Se14(SePh)36],[Cd32Se14(SePh)36-(PPh3) 4],[P(Et)2(Ph)C4H8OSiMe3]5 [Cd18I17(PSiMe3)12], and [N(Et)3C4H8OSiMe3]5[Cd18I17(PSiMe3)12]. *Angew. Chem. Int. Ed.* 1996, 35 (19), 2215–2218. https://doi.org/10.1002/anie.199622151.
- (20) Eichhöfer, A. Thermal Properties of [M10Se4(SePh) 12(PR3)4] (M = Zn, Cd, Hg) Cluster Molecules Synthesis and Structure of [Cd32Se14(SePh) 36(L)4]; L = OPPh3, OC4H8.
 Eur. J. Inorg. Chem. 2005, 1245–1253. https://doi.org/10.1002/ejic.200400799.
- (21) Soloviev, V. N.; Eichhofer, A.; Fenske, D.; Banin, U. Molecular Limit of a Bulk Semiconductor: Size Dependence of the "band Gap" in CdSe Cluster Molecules [15]. *J. Am. Chem. Soc.* **2000**, *122* (11), 2673–2674. https://doi.org/10.1021/ja9940367.

- Soloviev, V. N.; Eichhöfer, A.; Fenske, D.; Banin, U. Size-Dependent Optical Spectroscopy of a Homologous Series of CdSe Cluster Molecules. *J. Am. Chem. Soc.*2001, 123 (10), 2354–2364. https://doi.org/10.1021/ja003598j.
- (23) Beecher, A. N.; Yang, X.; Palmer, J. H.; Lagrassa, A. L.; Juhas, P.; Billinge, S. J. L.; Owen, J. S. Atomic Structures and Gram Scale Synthesis of Three Tetrahedral Quantum Dots. *J. Am. Chem. Soc.* **2014**, *136* (30), 10645–10653. https://doi.org/10.1021/ja503590h.
- (24) Cossairt, B. M.; Owen, J. S. CdSe Clusters: At the Interface of Small Molecules and Quantum Dots. *Chem. Mater.* **2011**, *23* (12), 3114–3119. https://doi.org/10.1021/cm2008686.
- (25) Fritzinger, B.; Capek, R. K.; Lambert, K.; Martins, J. C.; Hens, Z. Utilizing Self-Exchange to Address the Binding of Carboxylic Acid Ligands to CdSe Quantum Dots. *J. Am. Chem. Soc.* **2010**, *132* (29), 10195–10201. https://doi.org/10.1021/ja104351q.
- (26) Liu, Y. H.; Wang, F.; Wang, Y.; Gibbons, P. C.; Buhro, W. E. Lamellar Assembly of Cadmium Selenide Nanoclusters into Quantum Belts. *J. Am. Chem. Soc.* **2011**, *133* (42), 17005–17013. https://doi.org/10.1021/ja206776g.
- (27) Wang, Y.; Liu, Y. H.; Zhang, Y.; Wang, F.; Kowalski, P. J.; Rohrs, H. W.; Loomis, R. A.; Gross, M. L.; Buhro, W. E. Isolation of the Magic-Size CdSe Nanoclusters [(CdSe)13(n-Octylamine)13] and [(CdSe)13(Oleylamine) 13]. *Angew. Chem. Int. Ed.* **2012**, *51* (25), 6154–6157. https://doi.org/10.1002/anie.201202380.
- (28) Joo, J.; Son, J. S.; Kwon, S. G.; Yu, J. H.; Hyeon, T. Low-Temperature Solution-Phase Synthesis of Quantum Well Structured CdSe Nanoribbons. *J. Am. Chem. Soc.* **2006**, *128* (17), 5632–5633. https://doi.org/10.1021/ja0601686.
- (29) Yu, J. H.; Liu, X.; Kweon, K. E.; Joo, J.; Park, J.; Ko, K. T.; Lee, D. W.; Shen, S.; Tivakornsasithorn, K.; Son, J. S.; Park, J. H.; Kim, Y. W.; Hwang, G. S.; Dobrowolska, M.; Furdyna, J. K.; Hyeon, T. Giant Zeeman Splitting in Nucleation-Controlled Doped CdSe:Mn2+ Quantum Nanoribbons. *Nat. Mater.* **2010**, *9* (1), 47–53. https://doi.org/10.1038/nmat2572.
- (30) Bootharaju, M. S.; Baek, W.; Deng, G.; Singh, K.; Voznyy, O.; Zheng, N.; Hyeon, T. Structure of a Subnanometer-Sized Semiconductor Cd14Se13 Cluster. *Chem* **2022**, *8* (11) 2978–2989. https://doi.org/10.1016/j.chempr.2022.06.025.
- (31) Kasuya, A.; Sivamohan, R.; Barnakov, Y. A.; Dmitruk, I. M.; Nirasawa, T.; Romanyuk,

- V. R.; Kumar, V.; Mamykin, S. V.; Tohji, K.; Jeyadevan, B.; Shinoda, K.; Kudo, T.; Terasaki, O.; Liu, Z.; Belosludov, R. V.; Sundararajan, V.; Kawazoe, Y. Ultra-Stable Nanoparticles of CdSe Revealed from Mass Spectrometry. *Nat. Mater.* **2004**, *3* (2), 99–102. https://doi.org/10.1038/nmat1056.
- (32) Wang, Y.; Zhang, Y.; Wang, F.; Giblin, D. E.; Hoy, J.; Rohrs, H. W.; Loomis, R. A.; Buhro, W. E. The Magic-Size Nanocluster (CdSe)34 as a Low-Temperature Nucleant for Cadmium Selenide Nanocrystals; Room-Temperature Growth of Crystalline Quantum Platelets. *Chem. Mater.* **2014**, *26* (7), 2233–2243. https://doi.org/10.1021/cm404068e.
- (33) Dolai, S.; Nimmala, P. R.; Mandal, M.; Muhoberac, B. B.; Dria, K.; Dass, A.; Sardar, R. Isolation of Bright Blue Light-Emitting CdSe Nanocrystals with 6.5 KDa Core in Gram Scale: High Photoluminescence Efficiency Controlled by Surface Ligand Chemistry. *Chem. Mater.* **2014**, *26* (2), 1278–1285. https://doi.org/10.1021/cm403950f.
- (34) Nevers, D. R.; Williamson, C. B.; Savitzky, B. H.; Hadar, I.; Banin, U.; Kourkoutis, L. F.; Hanrath, T.; Robinson, R. D. Mesophase Formation Stabilizes High-Purity Magic-Sized Clusters. *J. Am. Chem. Soc.* **2018**, *140* (10), 3652–3662. https://doi.org/10.1021/jacs.7b12175.
- (35) Harrell, S. M.; McBride, J. R.; Rosenthal, S. J. Synthesis of Ultrasmall and Magic-Sized CdSe Nanocrystals. *Chem. Mater.* **2013**, *25* (8), 1199–1210. https://doi.org/10.1021/cm303318f.
- (36) Calvin, J. J.; Kaufman, T. M.; Sedlak, A. B.; Crook, M. F.; Alivisatos, A. P. Observation of Ordered Organic Capping Ligands on Semiconducting Quantum Dots via Powder X-Ray Diffraction. *Nat. Commun.* **2021**, 12:2663. https://doi.org/10.1038/s41467-021-22947-x.
- (37) Bowers, M. J.; McBride, J. R.; Garrett, M. D.; Sammons, J. A.; Dukes, A. D.; Schreuder, M. A.; Watt, T. L.; Lupini, A. R.; Pennycook, S. J.; Rosenthal, S. J. Structure and Ultrafast Dynamics of White-Light-Emitting CdSe Nanocrystals. *J. Am. Chem. Soc.* 2009, 131 (16), 5730–5731. https://doi.org/10.1021/ja900529h.
- (38) Hens, Z.; Martins, J. C. A Solution NMR Toolbox for Characterizing the Surface Chemistry of Colloidal Nanocrystals. *Chem. Mater.* **2013**, *25* (8), 1211–1221. https://doi.org/10.1021/cm303361s.
- (39) Juhás, P.; Davis, T.; Farrow, C. L.; Billinge, S. J. L. PDFgetX3: A Rapid and Highly

- Automatable Program for Processing Powder Diffraction Data into Total Scattering Pair Distribution Functions. *J. Appl. Crystallogr.* **2013**, *46* (2), 560–566. https://doi.org/10.1107/S0021889813005190.
- (40) Juhás, P.; Farrow, C. L.; Yang, X.; Knox, K. R.; Billinge, S. J. L. Complex Modeling: A Strategy and Software Program for Combining Multiple Information Sources to Solve Ill Posed Structure and Nanostructure Inverse Problems. *Acta Crystallogr. Sect. A Found. Adv.* 2015, 71, 562–568. https://doi.org/10.1107/S2053273315014473.
- (41) Gary, D. C.; Flowers, S. E.; Kaminsky, W.; Petrone, A.; Li, X.; Cossairt, B. M. Single-Crystal and Electronic Structure of a 1.3 Nm Indium Phosphide Nanocluster. *J. Am. Chem. Soc.* **2016**, *138* (5), 1510–1513. https://doi.org/10.1021/jacs.5b13214.
- Williamson, C. B.; Nevers, D. R.; Nelson, A.; Hadar, I.; Banin, U.; Hanrath, T.; Robinson,
 R. D. Chemically Reversible Isomerization of Inorganic Clusters. *Science* (80-.). 2019,
 363 (6428), 731–735. https://doi.org/10.1126/science.aau9464.
- (43) Frisch, M. J.; Trucks, G. W.; Schlegel, H. B.; Scuseria, G. E.; Robb, M. A.; Cheeseman, J. R.; Scalmani, G.; Barone, V.; Petersson, G. A.; Nakatsuji, H.; Li, X.; Caricato, M.; Marenich, A. V.; Bloino, J.; Janesko, B. G.; Gomperts, R.; Mennucci, B.; Hratchian, H. P.; Ortiz, J. V.; Izmaylov, A. F.; Sonnenberg, J. L.; Williams-Young, D.; Ding, F.; Lipparini, F.; Egidi, F.; Goings, J.; Peng, B.; Petrone, A.; Henderson, T.; Ranasinghe, D.; Zakrzewski, V. G.; Gao, J.; Rega, N.; Zheng, G.; Liang, W.; Hada, M.; Ehara, M.; Toyota, K.; Fukuda, R.; Hasegawa, J.; Ishida, M.; Nakajima, T.; Honda, Y.; Kitao, O.; Nakai, H.; Vreven, T.; Throssell, K.; Montgomery, J. A., J.; Peralta, J. E.; Ogliaro, F.; Bearpark, M. J.; Heyd, J. J.; Brothers, E. N.; Kudin, K. N.; Staroverov, V. N.; Keith, T. A.; Kobayashi, R.; Normand, J.; Raghavachari, K.; Rendell, A. P.; Burant, J. C.; Iyengar, S. S.; Tomasi, J.; Cossi, M.; Millam, J. M.; Klene, M.; Adamo, C.; Cammi, R.; Ochterski, J. W.; Martin, R. L.; Morokuma, K.; Farkas, O.; Foresman, J. B.; Fox, D. J. Gaussian 16, Revision A.03. Gaussian, Inc.: Wallingford, CT 2016.
- (44) Schnitzenbaumer, K. J.; Labrador, T.; Dukovic, G. Impact of Chalcogenide Ligands on Excited State Dynamics in CdSe Quantum Dots. *J. Phys. Chem. C* **2015**, *119* (23), 13314–13324. https://doi.org/10.1021/acs.jpcc.5b02880.
- (45) Klimov, V. I.; McBranch, D. W. Femtosecond 1P-to-1S Electron Relaxation in Strongly Confined Semiconductor Nanocrystals. *Phys. Rev. Lett.* **1998**, *80* (18), 4028–4031.

- https://doi.org/10.1103/PhysRevLett.80.4028.
- (46) Klimov, V. I. Spectral and Dynamical Properties of Multiexcitons in Semiconductor Nanocrystals. *Annu. Rev. Phys. Chem.* 2007, 58, 635–673. https://doi.org/10.1146/annurev.physchem.58.032806.104537.
- (47) Kwon, Y.; Oh, J.; Lee, E.; Lee, S. H.; Agnes, A.; Bang, G.; Kim, J.; Kim, D.; Kim, S. Evolution from Unimolecular to Colloidal-Quantum-Dot-like Character in Chlorine or Zinc Incorporated InP Magic Size Clusters. *Nat. Commun.* 2020, 11:3127.. https://doi.org/10.1038/s41467-020-16855-9.
- (48) Schnitzenbaumer, K. J.; Dukovic, G. Comparison of Phonon Damping Behavior in Quantum Dots Capped with Organic and Inorganic Ligands. *Nano Lett.* **2018**, *18* (6), 3667–3674. https://doi.org/10.1021/acs.nanolett.8b00800.
- (49) Mork, A. J.; Lee, E. M. Y.; Dahod, N. S.; Willard, A. P.; Tisdale, W. A. Modulation of Low-Frequency Acoustic Vibrations in Semiconductor Nanocrystals through Choice of Surface Ligand. *J. Phys. Chem. Lett.* 2016, 7 (20), 4213–4216. https://doi.org/10.1021/acs.jpclett.6b01659.
- (50) Lee, E. M. Y.; Mork, A. J.; Willard, A. P.; Tisdale, W. A. Including Surface Ligand Effects in Continuum Elastic Models of Nanocrystal Vibrations. *J. Chem. Phys.* **2017**, *147*, 044711. https://doi.org/10.1063/1.4995439.
- (51) Sagar, D. M.; Cooney, R. R.; Sewall, S. L.; Dias, E. A.; Barsan, M. M.; Butler, I. S.; Kambhampati, P. Size Dependent, State-Resolved Studies of Exciton-Phonon Couplings in Strongly Confined Semiconductor Quantum Dots. *Phys. Rev. B - Condens. Matter Mater. Phys.* 2008, 77, 235321. https://doi.org/10.1103/PhysRevB.77.235321.
- (52) Tyagi, P.; Cooney, R. R.; Sewall, S. L.; Sagar, D. M.; Saari, J. I.; Kambhampati, P. Controlling Piezoelectric Response in Semiconductor Quantum Dots via Impulsive Charge Localization. *Nano Lett.* 2010, 10 (8), 3062–3067. https://doi.org/10.1021/nl101605r.
- (53) Mule, A. S.; Mazzotti, S.; Rossinelli, A. A.; Aellen, M.; Prins, P. T.; Van Der Bok, J. C.; Solari, S. F.; Glauser, Y. M.; Kumar, P. V.; Riedinger, A.; Norris, D. J. Unraveling the Growth Mechanism of Magic-Sized Semiconductor Nanocrystals. *J. Am. Chem. Soc.* 2021, 143 (4), 2037–2048. https://doi.org/10.1021/jacs.0c12185.
- (54) Gary, D. C.; Petrone, A.; Li, X.; Cossairt, B. M. Investigating the Role of Amine in InP

- Nanocrystal Synthesis: Destabilizing Cluster Intermediates by Z-Type Ligand Displacement. *Chem. Commun.* **2017**, *53* (1), 161–164. https://doi.org/10.1039/C6CC07952K.
- (55) Evans, C. M.; Evans, M. E.; Krauss, T. D. Mysteries of TOPSe Revealed: Insights into Quantum Dot Nucleation. *J. Am. Chem. Soc.* **2010**, *132* (32), 10973–10975. https://doi.org/10.1021/ja103805s.
- (56) Newton, J. C.; Ramasamy, K.; Mandal, M.; Joshi, G. K.; Kumbhar, A.; Sardar, R. Low-Temperature Synthesis of Magic-Sized Cdse Nanoclusters: Influence of Ligands on Nanocluster Growth and Photophysical Properties. *J. Phys. Chem. C* **2012**, *116* (7), 4380–4389. https://doi.org/10.1021/jp2086818.
- (57) He, L.; Luan, C.; Liu, S.; Chen, M.; Rowell, N.; Wang, Z.; Li, Y.; Zhang, C.; Lu, J.; Zhang, M.; Liang, B.; Yu, K. Transformations of Magic-Size Clusters via Precursor Compound Cation Exchange at Room Temperature. *J. Am. Chem. Soc.* **2022**, *144* (41), 19060–19069. https://doi.org/10.1021/jacs.2c07972.

TOC Graphic

